Journal of the Meteorological Society of Japan

EARLY ONLINE RELEASE

This is a PDF of a manuscript that has been peer-reviewed and accepted for publication. As the article has not yet been formatted, copy edited or proofread, the final published version may be different from the early online release.

This pre-publication manuscript may be downloaded, distributed and used under the provisions of the Creative Commons Attribution 4.0 International (CC BY 4.0) license. It may be cited using the DOI below.

The DOI for this manuscript is
DOI:10.2151/jmsj.2025-006
J-STAGE Advance published date: November 13, 2024
The final manuscript after publication will replace the preliminary version at the above DOI once it is available.

A statistical study of gravity waves in the troposphere and lower stratosphere in the Antarctic based on the PANSY radar observations

Eiji TOKIMORI[1]

Department of Earth and Planetary Science
The University of Tokyo, Tokyo, Japan

Masashi KOHMA

Department of Earth and Planetary Science
The University of Tokyo, Tokyo, Japan

and

Kaoru SATO

Department of Earth and Planetary Science
The University of Tokyo, Tokyo, Japan

February 29, 2024

----

1) Corresponding author: Eiji Tokimori, Department of Earth and Planetary Science, The University of Tokyo, 7-3-1 Hongo, Bunkyo, Tokyo 113-0033 JAPAN
Email: tokimori@eps.s.u-tokyo.ac.jp
Tel: +81-3-5841-4296

Abstract

Using observational data from the Program of the Antarctic Syowa Mesosphere-Stratosphere-Troposphere/Incoherent Scatter radar (PANSY radar) at Syowa Station (69.0°S, 39.6°E) over seven years, the climatology of gravity wave (GW) characteristics in the troposphere and lower stratosphere in the Antarctic were examined.

Our analysis shows that the GW kinetic energy in the lower stratosphere is consistent with previous studies using operational radiosonde observations in the Antarctic, including an enhancement during austral spring. We derive a theoretical formula relating horizontal and vertical wind contributions to the GW kinetic energy with the GW intrinsic frequency and the aspect ratio. The vertical variation of the intrinsic frequency suggests the presence of GW sources near the tropopause in addition to those in the troposphere and near the ground. The GW momentum fluxes estimated from radar data indicate that net GW forcing is eastward in the lower stratosphere in seasons except for summer, which acts to accelerate the lower part of the polar night jet. Furthermore, we present the climatology of Eulerian-mean vertical winds elucidated from the long-term radar observations.

Keywords gravity wave; Antarctic; troposphere-lower stratosphere; VHF radar

1. Introduction

Gravity waves (GWs) are atmospheric waves whose restoring force is buoyancy. Compared to Rossby waves, GWs have small temporal and spatial scales. Through vertical transport of horizontal momentum, GWs are known to play important roles in determining the position and strength of the zonal wind jets (Palmer et al., 1986; McFarlane, 1987). In addition, GWs largely contribute to the formation of the stratospheric and mesospheric general circulation (e.g., Plumb, 2002; Alexander et al., 2010) and equatorial zonal-mean zonal wind oscillations such as the quasi-biennial oscillation (QBO) (e.g., Sato and Dunkerton, 1997; Baldwin et al., 2001; Ern et al., 2014). In the Southern Hemisphere, upward propagating GWs which originate from the troposphere tend to converge toward the polar night jet (Sato et al., 2009; Amemiya and Sato, 2016; Kogure et al., 2018). This is considered one of the processes which is essential to mitigate the cooling bias in the polar stratosphere and the delay bias of the polar vortex breakdown in climate models (McLandress et al., 2012).

GWs in the Antarctic have been studied using observations from radiosondes, satellites, and radars as well as numerical model simulations (e.g., Pfenninger et al., 1999; Yoshiki and Sato, 2000; Alexander and Teitelbaum, 2007; Sato and Yoshiki, 2008; Jewtoukoff et al., 2015; Alexander and Murphy 2015; Yoo et al., 2018; Kruse et al., 2022). For Syowa Station (69.0°S, 39.6°E), Yoshiki et al. (2004) examined the seasonal variation of kinetic and potential energies of GWs in the troposphere and lower stratosphere from operational radiosonde observations. Program of Antarctic Syowa Mesosphere-Stratosphere-Troposphere/Incoherent Scatter (MST/IS) radar (the PANSY radar; Sato et al., 2014) at Syowa Station, which is the first large VHF clear-air Doppler radar in the Antarctic, has been continuously operated with its full system of the radar since 30 September 2015. Using the PANSY radar data, dynamical characteristics of Antarctic GWs have been examined for the troposphere and lower stratosphere (e.g., Mihalikova et al., 2016; Minamihara et al., 2018; 2020) and for the upper mesosphere (e.g., Sato et al., 2017; Shibuya et al., 2017). Using continuous data from the PANSY radar for one year from October 2015 to September 2016, Minamihara et al. (2018) showed the dominance of near-inertial frequency GWs in the lower stratosphere in all seasons and Minamihara et al. (2020) demonstrated larger GW intermittency in the troposphere than in the lower stratosphere.

This study aims to clarify the climatology of the GW characteristics including momentum fluxes and kinetic energy in the troposphere and lower stratosphere in the Antarctic using the PANSY radar observations over seven years from October 2015–September 2022. Seasonal variations of the mean winds including vertical winds, which can be accurately estimated only by the large atmospheric radars, are also shown first for the Antarctic. In addition, we derive a theoretical formula which relates statistically the intrinsic frequency with the ratio of horizontal to vertical wind contributions to the GW kinetic energy, apply it to the radar data, and show the seasonal change of the intrinsic frequency.

This paper is organized as follows: the PANSY radar observations and methods to estimate the intrinsic frequency are described in section 2. Section 3 shows the climatology of GW characteristics as well as that of the background field of wind and Brunt-Väisälä frequency squared. The seasonal variation of the GW characteristics is discussed in section 4. Last, the summary and concluding remarks are provided in section 5.

2. Data and Methodology

The PANSY radar is a pulse-modulated monostatic Doppler radar system operated at 47 MHz and consists of 1045 crossed-Yagi antennas (Sato et al., 2014). A standard observation mode uses five beams pointing vertically and obliquely to the north, east, south, and west at a zenith angle of 10°. This radar receives scattering echo from atmospheric turbulence which ubiquitously exist in the atmosphere, although the strength depends on the case. The radar observes radial wind velocities with a range resolution of 150 m and a temporal resolution of about 90 s. In the present study, the data obtained from the echo spectra integrated over every 30 min are used (Sato et al., 1997). Note that this integration makes the analysis insensitive to the fluctuations with wave periods shorter than approximately 1 hour.

The radar horizontal winds were estimated from the radial velocities by assuming the uniformity of the wind field between the two symmetric beams. The radial velocities of the east beam V_{E} and the west beam V_{W} with zenith angles $\pm\theta$ are expressed using the zonal wind u and vertical wind w,

$$V_{\mathrm{E}} = u \sin\theta + w \cos\theta \,, V_{\mathrm{W}} = -u \sin\theta + w \cos\theta$$

Thus, u can be estimated using V_{E} and V_{W}

$$u = \frac{V_{\mathrm{E}} - V_{\mathrm{W}}}{2\sin\theta}(2)$$

The meridional winds v are calculated similarly. The vertical winds w are directly estimated from the vertical beam. In the following analysis, two types of disturbances extracted by a high-pass filter are examined, namely, short wave period GWs and short vertical wavelength GWs. The former is defined as fluctuations with wave periods shorter than 1 day, while the latter as fluctuations with vertical wavelengths shorter than 6 km. Note that, while short period GWs are often defined as waves with a period shorter than a few hours, in the present study, the term “short wave period GW” is used to refer to high-frequency components, contrasting with the definition of GWs based on the vertical wavelength. These two types of high-pass filter have advantages respectively. In the former, many of the same GWs can be analyzed at different altitudes through a focus on wave periods, assuming that wave periods do not vary greatly. Disturbances with ground-based phase velocities are close to zero such as orographic GWs cannot be extracted. On the other hand, zero phase speed disturbances are extracted in the latter. Figure 1 shows the Fig. 1 time-height sections of the unfiltered u and w and the two types of GW fluctuations near the tropopause ($z =$ ~10 km). Wave patterns in the height range of 14–17 km are generally similar for short wave period and short vertical wavelength GWs. On the other hand, below 14km, the wave patterns filtered by each method are quite different. Wavelike disturbances with vertical wavelengths shorter than 6 km and wave periods longer than 1 day are dominant in the horizontal wind fields (Figs. 1e and to a lesser extent Fig. 1f), while disturbances with almost vertically aligned but slightly tilted phase structures with large amplitudes are observed particularly below $z = \sim 13$ km only in the short wave period GWs. The background fields are calculated as the components with vertical wavelengths longer than 6 km and wave periods longer than 1 day. Hereinafter, disturbance which are extracted by using high-pass filter in temporal or vertical direction and the background field of a physical quantity A are denoted as A', $A^{\dagger}$, and $\overline{A}$, respectively. In the following, we use prime when describing examples of quantities which include disturbances. The prime in these explanations can be replaced with a dagger, and the same can be considered for short vertical wavelength GWs.

Vertical fluxes of zonal and meridional momentum are estimated using the method proposed by Vincent and Reid (1983). Assuming uniformity of statistical properties of disturbances such as variances and covariances at a certain height, the vertical flux of zonal momentum per unit mass $\overline{u'w'}$ is estimated by

$$\overline{u'w'} = \frac{\overline{V_{\mathrm{E}}'^2} - \overline{V_{\mathrm{W}}'^2}}{2 \sin 2\theta} \quad (3)$$

The vertical flux of meridional momentum $\overline{v'w'}$ is calculated similarly.

Figure 2 shows the percentage of available data from the vertical beam and the average percentage from the four oblique beams as a function of height. In the following, the climatology is shown only for the heights where the available data percentage is larger than

Fig. 2

60 %. In other words, vertical winds are obtained for the height range from 1.5 to 25 km, while horizontal winds and momentum fluxes are obtained from 1.5 to 22 km.

The Brunt-Väisälä frequency N is calculated from radiosonde observations at Syowa Station, which are made twice daily by the Japan Meteorological Agency.

To obtain the climatology of GW characteristics, the following procedures were preformed: First, by dividing each month into 6 time periods, a 5-day mean was calculated for each quantity. The data on the 31 of January, March, May, July, August, October, December are included to make the last 5-day mean of each month. The last 5-day mean for February was calculated using data of the 26–28th of February or of the 26–29th of February depending on the year. Next, the time series of the 5-day mean data were averaged over seven years. Last, a one-month running mean was made in time and then a 500-m running mean was made in the vertical.

Many previous studies examine GW characteristics such as intrinsic frequency $\hat{\omega}$ using observations with high vertical resolutions from radiosondes and MST radars by analyzing hodographs assuming a monochromatic wave for each short vertical range (e.g., Hirota and Niki, 1985; Sato and Yoshiki, 2008; Minamihara et al., 2018). In the present study, by taking advantage of the capability to observe the vertical wind directly, a theoretical formula was newly derived to estimate the intrinsic frequency statistically. First, the ratio of the kinetic energy due to the vertical winds ($\mathrm{KE}_{(z)} \equiv \frac{1}{2}\rho_0 \overline{w'^2}$) to that due to horizontal winds ($\mathrm{KE}_{(\mathrm{h})} \equiv \frac{1}{2}\rho_0 \left(\overline{u'^2} + \overline{v'^2}\right)$) is defined as

$$R \equiv \frac{\overline{w'^2}}{\overline{u'^2} + \overline{v'^2}} \quad (4)$$

The relation between the horizontal wind component parallel to ($u_\parallel$) and that perpendicular to ($u_\perp$) the wavenumber vector of an inertia-GW is expressed as

$$|u_\parallel| = \left|\frac{\hat{\omega}}{f} u_\perp\right| \quad (5)$$

Using the dispersion relation for non-hydrostatic inertia-GWs (Fritts and Alexander, 2003)

$$\left(\frac{k}{m}\right)^2 = \frac{\hat{\omega}^2 - f^2}{N^2 - \hat{\omega}^2} \quad (6)$$

$ku_\parallel + mw' = 0$ derived from the equation of continuity, and $\overline{u'^2} + \overline{v'^2} = \overline{u_\parallel{}^2} + \overline{u_\perp{}^2}$, R is expressed as

$$R = \left[1 + \left(\frac{f}{\hat{\omega}}\right)^2\right]^{-1} \cdot \frac{1 - \left(\frac{f}{\hat{\omega}}\right)^2}{\left(\frac{f}{\hat{\omega}}\right)^2 - \left(\frac{f}{N}\right)^2} \cdot \left(\frac{f}{N}\right)^2 \quad (7)$$

Then, $|f/\hat{\omega}|$ is obtained as

$$\left|\frac{f}{\hat{\omega}}\right| = \sqrt{\frac{2(R+1)}{1 + R(\tilde{N}^2 - 1) + \sqrt{\left[1 + R(\tilde{N}^2 - 1)\right]^2 + 4(R+1)R\tilde{N}^2}}} \quad (8)$$

where

$$\tilde{N} \equiv \frac{N}{f}. \quad (9)$$

In addition, $|k/m|$ is expressed by using $\left|\frac{f}{\hat{\omega}}\right|$ as

$$\left|\frac{k}{m}\right| = \sqrt{R\left(1 + \left|\frac{f}{\hat{\omega}}\right|^2\right)} \quad (10)$$

3. Results

Figure 3 shows the time-height sections of the climatology of background fields of (a) zonal wind $\overline{u}$, (b) meridional wind $\overline{v}$, (c) vertical wind $\overline{w}$, and (d) Brunt-Väisälä frequency squared N^2 along with the tropopause for the temperature climatology. The $\overline{u}$ values tend to be negative below the height of $z = {\sim}3$ km and positive above $z =$ ~9 km. Westerly winds are stronger as height increases. The westerly winds are faster than 20 m s^{-1} above $z =$ ~15 km from April to November. The westerly wind takes a maximum near the top of the displayed height range, with a value of about 40 m s^{-1}. The height of $\overline{u} = 0$ m s^{-1}, which is the critical level of zonally propagating orographic gravity waves, is higher in summer than in other seasons. The maximum height of the critical level is slightly higher than $z = {\sim}9$ km in summer. The $\overline{v}$ values are generally negative, but positive values are observed in autumn and spring in the height range of ~15–20 km. Northerly winds are strong around $z =$ ~20 km and reach 10 m s^{-1} or more in October. Sharp changes exist near $z =$ ~20 km, where the number of effective observation points is less than in lower altitudes. The effect of the effective observation points still remains in the 500-m vertical smoothing. Note, however, that if the smoothing range is increased to eliminate this effect, the vertical profile cannot be examined in detail. The $\overline{w}$ values in the troposphere are generally positive and especially large at $z < {\sim}4$ km. In the height range of 13–25 km, $\overline{w}$ values are mainly negative from January to March, with a minimum value of ~-11 mm/s, whereas they are strongly positive from June to November, with a maximum value of ~43 mm s^{-1}. The

Fig. 3

tropopause is located at a height within 8–10 km from December to June and within 9–13 km from July to November. A local maximum in N^2 values occur at $z =$ ~10 km from January to April. In addition, the region with large N^2 gradually descends from higher altitudes in spring.

Figure 4 shows the climatology of $\overline{u'w'}$, $\overline{v'w'}$, kinetic energy due to horizontal wind fluctuations $\mathrm{KE}_{(\mathrm{h})}$ and to vertical wind fluctuations $\mathrm{KE}_{(z)}$, R, $|f/\hat{\omega}|$, and $|k/m|$ for the short wave period GWs in time-height sections. Here, the basic density $\rho_0(z)$ is given by $\rho_s e^{-\frac{z}{H}}$, where H and ρ_s are 7 km and 1.3 kg m^{-3}, respectively. Fig. 4

The $\overline{u'w'}$ values are strongly negative from March to November in the height range of ~12–22 km in the lower stratosphere, where strong westerly winds are observed (Figure 4a). In December to February, $\overline{u'w'}$ is quite weak in the weak mean zonal wind. In contrast, in the troposphere, $\overline{u'w'}$ tends to be positive in $z =$ 3–10 km, while negative below throughout the year. The $\overline{v'w'}$ values are negative in most of the height region of $z =$ 1.5–5 km throughout the year (Figure 4b). The negative $\overline{u'w'}$ and negative $\overline{v'w'}$ in the lower troposphere are consistent with orographically generated GWs in the southwestward mean wind which is dominant at Syowa Station (Sato and Hirasawa, 2007). An interesting correspondence between $\overline{v'w'}$ and $\bar{v}$ is observed in $z =$ 10–20 km in the stratosphere: $\overline{v'w'}$ is positive (negative) when $\bar{v}$ is negative (positive).

The $\mathrm{KE}_{(\mathrm{h})}$ values in the troposphere ($z <$ ~10km) are generally larger in winter than in summer, and ~1–3 kg m^{-1} s^{-2} (Figure 4c). The $\mathrm{KE}_{(\mathrm{h})}$ values in the lower stratosphere are less than 1 kg m^{-1} s^{-2}, which is smaller than those in the troposphere. An interesting feature is that $\mathrm{KE_{(h)}}$ is maximized in spring for $z = $ 15–20 km in the stratosphere where N^2 is maximized. This feature is consistent with results by previous studies based on radiosonde observations (Pfenninger et al. 1999; Yoshiki and Sato, 2000; Yoshiki et al. 2004). The $\mathrm{KE}_{(z)}$ values are quite large in the lower troposphere in all seasons especially in winter and spring from August to November, while the $\mathrm{KE}_{(z)}$ exhibits clear seasonal variation above $z =$ ~12 km in the stratosphere which is small in summer (December to February) and large in winter (April to October) (Figure 4c). Compared to the $\mathrm{KE_{(h)}}$, the $\mathrm{KE}_{(z)}$ has a sharp decrease with height around $z =$ ~ 11 km, which is reflected by the R minimum observed around $z =$ ~9 km (Figure 4e). In the height range of ~13–22 km in the lower stratosphere, R is large from March to November. The vertical profile of R is minimized around z=~9 km near the tropopause, which is especially obvious in March to April. The R value is largest at the observed lowest height (1.5 km).

Figure 4f shows seasonal variation of $f/\hat{\omega}$ obtained using Eq. (7). Note that $f/\hat{\omega}$ is proportional to intrinsic wave periods. The $f/\hat{\omega}$ value has a distinct seasonal variation in the height range of 15–22 km, taking a maximum of about 0.30 in summer and a minimum of about 0.11 in autumn and spring. In other words, the intrinsic wave periods are longer in summer and shorter in autumn and spring. The $f/\hat{\omega}$ value takes a maximum in the vertical slightly below the tropopause throughout the year and particularly evident from March to April whose largest value is 0.38. In contrast, the vertical profile of $f/\hat{\omega}$ has a minimum of

<0.1 near the observed lowest height of z=1.5 km throughout the year and also minimized at the observed highest height ($z=$ ~22 km) from May to November.

Figure 4g shows the climatology of k/m. Small k/m in the lower stratosphere in summer is consistent with the prominence of GWs with near-inertial frequencies (Minamihara et al., 2018). Large k/m observed in the troposphere is considered due to active orographic GWs. Increasing k/m with height in the lower stratosphere from April to October is interpreted as the GW oscillations being aligned more vertically in stronger westerly winds. The minimum of k/m near the troposphere indicates dominance of GWs with horizontally aligned oscillation surface compared to other altitudes.

Figures 5a and 5b respectively show the climatology of the vertical convergences of the vertical flux of zonal and meridional momentum $(\overline{X}, \overline{Y})$ $\left(\equiv\left(-\frac{1}{\rho_0}\frac{\partial \rho_0 \overline{u'w'}}{\partial z}, -\frac{1}{\rho_0}\frac{\partial \rho_0 \overline{v'w'}}{\partial z}\right)\right)$ for the short wave period GWs in a time-height section. For clear visualization, a 2-km running mean was made in the vertical. The $\overline{X}$ value tends to be positive in the height range of 9–17 km, which is particularly dominant in winter season from May to November having a mean value of ~0.37 m s^{-1} day^{-1}. In contrast, $\overline{Y}$ values above $z=$ 10 km in the lower stratosphere are not very large and weakly positive in May to August with an average value of ~0.24 m s^{-1} day^{-1} for $z=$ 12–14 km, while they tend to be negative in the troposphere.

Fig. 5

Figures 5c and 5d show annual-mean $\overline{X}$ and $\overline{Y}$ as a function of height with their standard deviations. In the height range of 11–17 km in the stratosphere, $\overline{X}$ is significantly positive, while $\overline{Y}$ is about 0 m s^{-1} day^{-1}. In the height range below 9 km in the troposphere, both $\overline{X}$

and $\overline{Y}$ tends to be negative, with large variation in the vertical. It is important that the standard deviation for both $\overline{X}$ and $\overline{Y}$ is quite large in the troposphere compared with that in the stratosphere, which is related to large intermittency of GWs in the troposphere (Minamihara et al., 2020).

Figure 6 shows results for the short vertical wavelength GWs. Since these GWs share similar characteristics with the short wave period GWs, only the differences in the climatological features between the two types of GWs are highlighted: (Fig. 6a) The $\overline{u^{\dagger}w^{\dagger}}$ values of the short vertical wavelength GWs are larger in $z =$ ~3–10 km than short wave period GWs. (Fig. 6b) The $\overline{v^{\dagger}w^{\dagger}}$ values of the short vertical wavelength GWs are generally smaller than short wave period GWs. (Fig. 6c) $\mathrm{KE}_{(\mathrm{h})}$ of the short vertical wavelength GWs is larger below $z =$ ~4 km but smaller in $z =$ ~7–10 km than short wave period GWs, especially in June through November. (Fig. 6d) $\mathrm{KE}_{(z)}$ of the short vertical wavelength GWs tends to be smaller in the entire displayed height range. (Fig. 6e) R of the short vertical wavelength GWs is generally smaller than short wave period GWs. Vertical change of R in $z >$ 10 km in the stratosphere is different between the two types of GWs: R of short vertical wavelength GWs does not change significantly with height, whereas that of short wave period GWs increases with height during winter and spring. (Fig. 6f) The $f/\hat{\omega}$ values for the short vertical wavelength GWs are generally larger especially in $z =$ 15–22 km from autumn to spring. In addition, $f/\hat{\omega}$ is maximized near the tropopause ($z =$ ~9 km) and amounts to 0.37 from January to April. (g) The aspect ratio k/m of the short vertical wavelength GWs

Fig. 6

is generally smaller than short wave period GWs.

4. Discussion

In this section, vertical and seasonal variations of observed GW characteristics in terms of $f/\hat{\omega}$, k/m, and the vertical flux of horizontal momentum are discussed.

In the lower stratosphere, $f/\hat{\omega}$ in summer is larger than that in winter. This seasonal variation is qualitatively consistent with the previous studies (Yoshiki et al., 2004; Mihalikova et al., 2016), although the $f/\hat{\omega}$ values in the present study are slightly smaller than those in previous studies, likely due to the differences in the definition of GW fluctuations and estimation methods of $f/\hat{\omega}$.

The $f/\hat{\omega}$ maximum near the tropopause is related to the $\mathrm{KE}_{(\mathrm{h})}$ maximum which leads to small R there. This means that the air oscillations associated with GWs are more horizontally tilted there. According to the dispersion relation, R of a monochromatic GW becomes smaller in a larger N^2 region. However, the R minimum is located not at the N^2 peak but slightly below. This feature indicates that the GWs having small R are not due to change in the upward propagation conditions and so do not come from the lower atmosphere but are generated there. A most plausible generation mechanism is spontaneous adjustment near the upper tropospheric jet (e.g., Hirota and Niki, 1985; Sato, 1994; Plougonven and Snyder, 2007; Yasuda et al., 2015a; 2015b). This can explain not only the small R, but the minimum of R, since the GWs radiated from the jet-front system do not propagate significantly in the vertical direction.

The partial reflection is known as one of the notable properties of GWs associated with sharp gradient of N^2 and might impact the vertical profiles of R around the tropopause. The relation between GW oscillation surfaces and transmission rates across the tropopause is summarized in Appendix. It demonstrates that GWs with an oscillation surface close to vertical are more prone to partial reflection compared to those with an oscillation surface close to horizontal. Thus, the partial reflection at the tropopause is expected to result in a small R above the tropopause. However, the present results show that R remains almost constant near the height of 9 km, where there is a large vertical gradient of N^2.This suggests that the partial reflection play an only secondary role in formation of the climatological vertical profiles of R.

In the height range of 15–22 km in the stratosphere, $f/\hat{\omega}$ values are smaller at higher altitudes from April to October. This feature is attributable to strong background westerly winds greater than 20 m s^{-1} from April to November (Fig. 3a). Because $\overline{u'w'}$ is negative there, GWs should have c smaller than $\overline{u}$. Hence, the absolute values of the intrinsic phase velocity $|\hat{c}|(=|c-\overline{u}|)$ and intrinsic frequency $|\hat{\omega}|(=|k\hat{c}|)$ are larger in the stronger westerly winds.

In the height range of 15–22 km, vertical increase in negative $\overline{u'w'}$ (Fig. 4a) and positive $\overline{X}$ (Fig. 5a) are observed except in summer. As an interpretation, the sign of the wave forcing can be explained by multiple upward propagating GWs having eastward and westward intrinsic phase velocities as an interpretation: A large part of GWs having eastward phase velocities relative to the background westerly winds having westerly shear are absorbed when they encounter the critical levels, while a remaining part of GWs having westward phase speeds relative to the background winds survive and freely propagate upward. The negative $\overline{u'w'}$ in the upper levels can be explained by the presence of latter GWs, whereas the positive $\overline{X}$ can be explained by the critical level filtering of the former GWs. This is also the first observational evidence showing that the GWs forcing is eastward and accelerates the lower part of the polar night jet.

In the lower stratosphere, $\mathrm{KE}_{(z)}$ for short wave period GWs increases with height during winter while that for short vertical wavelength GWs does not change significantly. This result means that GWs with long vertical wavelengths are more dominant at higher altitudes. This feature can also be explained by change in m of upward propagating GWs having westward intrinsic phase speeds in the strong westerly shear.

In the lower stratosphere, the increase of R for short wave period GWs with height is larger than that for short vertical wavelength GWs from May to October (Figs. 4e, 6e). In this region, GW oscillation surfaces relatively get vertical due to strong westerly shear, and vertical amplitudes increase. The R for short wave period GWs reflects this change and increases with height because the extraction by wave periods captures the same GWs. On the other hand, R for short vertical wavelength GWs does not increase significantly. This is likely because GWs with large R are no longer extracted due to the increase of vertical wavelength as vertical amplitudes increase.

5. Summary

A statistical analysis of the GWs in the troposphere and lower stratosphere has been performed based on the continuous data from the PANSY radar observations at Syowa Station in the Antarctic over seven years. The climatology of the background winds and characteristics of the two types of GWs, namely, GWs having short wave periods ($\tau \leq$ 1d) and short vertical wavelengths ($\lambda_z \leq$ 6 km) were obtained. The climatology of the mean vertical wind in the Antarctic is a result made possible only by the long continuous data for seven years from the PANSY radar.

In the height range of 13–25 km, the vertical winds are negative with a minimum value of -11 mm s^{-1} from late December to early March, while they are positive with a maximum value of 43 mm s^{-1} in remaining time periods. This feature is the first observational result for the Antarctic with the aid of the advantage of a large atmospheric radar and consistent with a general view of the Eulerian mean vertical winds at high latitudes shown by previous studies (e.g., Cunnold et al., 1975). It seems that upward winds are dominant in the troposphere although clear tendency in their sign is not observed. The kinetic energy of GWs in the height range of 15–22 km is maximized in austral spring, which is consistent with previous studies based on radiosonde observations. A diagnostic estimation of $f/\hat{\omega}$ taking advantage of the availability of both horizontal and vertical wind fluctuations was made by a newly proposed method in the present study. An interesting result is that $f/\hat{\omega}$ is maximized near the tropopause, suggesting GW generation from the tropopausal jet. A vertical profile of $\overline{u'w'}$ shows positive values in the lowermost stratosphere and negative ones above, which suggests the presence of multiple GWs causing strong eastward wave forcing in the lower part of the westerly polar night jet. The average of the eastward wave forcing amounts to about 0.37 m s^{-1} day^{-1} in the height range of 9–17 km from May to November.

The PANSY radar observations will continue until September 2027. It is also possible to examine interannual variation of GWs. It is important to investigate the GW horizontal propagation and the wave sources by combination with radar data at other locations and GW-permitting general circulation model simulations (e.g. Okui et al.,2021). The analysis of GWs in the mesosphere is important to investigate seasonal changes of GW characteristics and to elucidate the relation with stratospheric GWs based on the PANSY radar observations.

Data Availability Statement

The data from the PANSY radar is available from the PANSY Data Archive (https://pansy-data.nipr.ac.jp/pansyda/home/). The data from radiosonde observations is available at the JMA website (https://www.data.jma.go.jp/obd/stats/etrn/upper/index.php).

Acknowledgments

Operational radiosonde observations by JMA and the PANSY radar operation are made in the framework of Japanese Antarctic Research Expedition (JARE). We greatly appreciate the summer and wintering members of JARE. This work was supported by JSPS KAKENHI Grant JP22H00169 and JST FOREST JPMJFR2231.

Appendix

To Investigate the impact of partial reflection at the tropopause on the present results, the energy ratio of upward GW in the stratosphere which passed through the tropopause to the upward GWs in the troposphere (i.e., transmission rate) is obtained based on the analytical solution for GWs in two layers with different static stability. Following Sutherland and Yewchuk (2004), we consider small-amplitude waves in a stationary two-dimensional Boussinesq fluid under the assumption that the background winds are zero. The Brunt-Väisälä frequencies squared are given by constant values of N_{T}^2 and N_{S}^2 in the troposphere and stratosphere, respectively.

The small-amplitude waves are known to satisfy the following equation:

$$\left(\frac{\partial^2}{\partial x^2}+\frac{\partial^2}{\partial z^2}\right)\frac{\partial^2\psi}{\partial t^2}+N^2\frac{\partial^2\psi}{\partial x^2}=(A1)$$

where ψ is the streamfunciton for the waves. Solutions of (A1) are a superposition of $\psi=\hat{\psi}(z)\exp[i(kx-\omega t)]$, where $\hat{\psi}(z)$ in the troposphere ($z<0$) and stratosphere ($z>0$) are obtained as $\widehat{\psi_{\mathrm{T}}}=A_{\mathrm{T}}\exp\left(ik\sqrt{N_{\mathrm{T}}^2-\omega^2}z\right)+B_{\mathrm{T}}\exp\left(-ik\sqrt{N_{\mathrm{T}}^2-\omega^2}z\right)$ and $\widehat{\psi_{\mathrm{S}}}=A_{\mathrm{S}}\exp$

$\left(ik\sqrt{N_S^2-\omega^2}z\right)$, respectively. From continuity of pressure and vertical velocity across the tropopause ($z=0$), the transmission rate, is given by

$$\frac{A_S^2}{A_T^2}=\frac{4\left(N_T^2-\omega^2\right)}{\left(\sqrt{N_T^2-\omega^2}+\sqrt{N_S^2-\omega^2}\right)^2}\text{(A2)}$$

We define $\Theta_T=\arccos\left(\frac{\omega}{N_T}\right)$, which indicates the angle between phase line of GWs and the vertical direction. Using the dispersion rate of internal GWs $\omega^2=N^2k^2/(k^2+m^2)$, the transmission rate is rewritten as

$$\frac{A_S^2}{A_T^2}=\frac{4\sin^2\Theta_T}{\left(\sin\Theta_T+\sqrt{N_S^2/N_T^2-\cos^2\Theta_T}\right)^2}\text{(A3)}$$

The transmission rate increases with Θ_T in the range of $0<\Theta_T<\frac{\pi}{2}$, and GWs with an oscillation surface close to vertical are prone to partial reflection. Sato et al. (2012) derived the formulation of partial reflection rates using the dispersion relation of hydrostatic inertia-GWs: $(N_S-N_T)/(N_S+N_T)$. The equation is rewritten to the transmission rate:

$$\frac{A_S^2}{A_T^2}=\frac{4N_T^2}{(N_S+N_T)^2}\text{(A4)}$$

Note that, for $\omega^2\ll N_T^2, N_S^2$ (low-frequency waves), (A3) is equivalent to (A4).

References

Alexander, M. J., M Geller., C. McLandress, S. Polavarapu, P. Preusse, F Sassi, K. Sato, S. Eckermann, M. Ern, A. Hertzog, Y. Kawatani, M. Pulido, T. A. Shaw, M. Sigmond, R. Vincent, and S. Watanabe, 2010: Recent developments in gravity-wave effects in climate models and the global distribution of gravity-wave momentum flux from observations and models. *Quart. J. Roy. Meteor. Soc.*, **136**, 1103–1124. doi:10.1002/qj.637.

Alexander, M. J., and M. Teitelbaum, 2007: Observation and analysis of a large amplitude mountain wave event over the Antarctic peninsula. *J. Geophys. Res.: Atmos.*, **112**, D21. doi:10.1029/2006JD008368.

Alexander, S., and D. Murphy, 2015: The seasonal cycle of lower-tropospheric gravity wave activity at Davis, Antarctica (69°S, 78°E). *J. Atmos. Sci.*, **72(3)**, 1010–1021. doi:10.1175/JAS-D-14-0171.1.

Amemiya, A., and K. Sato, 2016: A new gravity wave parameterization including three-dimensional propagation. *J. Meteor. Soc. Japan Ser. II*, **94(3)**, 237–256. doi:10.2151/jmsj.2016-013.

Baldwin, M., L. Gray, T. Dunkerton, K. Hamilton, P. Haynes, W. Randel, M. Alexander, I. Hirota, T. Horinouchi, D. Jones, J. Kinnersley, C. Marquardt, K. Sato, and M. Takahashi, 2001: The quasi-biennial oscillation. *Rev. Geophys.*, **39(2)**, 179–229. doi:10.1029/1999RG000073.

Cunnold, D., F. Alyea, N. Phillips, and R. Prinn, 1975: A three-dimensional dynamical-chemical model of atmospheric ozone. *J. Atmos. Sci.*, **32**, 170–194, doi:10.1175/1520-0469(1975)032<0170:ATDDCM>2.0.CO;2.

Ern, M., F. Ploeger, P. Preusse, J. C. Gille, L. J. Gray, S. Kalisch, M. G. Mlynczak, J. M. Russell III, and M. Riese, 2014: Interaction of gravity waves with the QBO: A satellite perspective. *J. Geophys. Res.: Atmos.*, **119(5)**, 2329–2355. doi:10.1002/2013JD020731.

Fritts, D. C., and M. J. Alexander, 2003: Gravity wave dynamics and effects in the middle atmosphere. *Rev. Geophys.*, **41(1)**, 1003. doi:10.1029/2001RG000106.

Hertzog, A., M. J. Alexander, and R. Plougonven, 2012: On the intermittency of gravity wave momentum flux in the stratosphere. *J. Atmos. Sci.*, **69(11)**, 3433–3448. doi:10.1175/JAS-D-12-09.1.

Hirota, I., and T. Niki, 1985: A statistical study of inertia-gravity waves in the middle atmosphere. *J. Meteor. Soc. Japan Ser. II*, **63(6)**, 1055–1066. doi:10.2151/jmsj1965.63.6_1055.

Jewtoukoff, V., A. Hertzog, R. Plougonven, A. Cámara, and F. Lott, 2015: Gravity waves in the Southern Hemisphere derived from balloon observations and ECMWF analyses. *J. Atmos. Sci.*, **72**, 3449–3468. doi:10.1175/JAS-D-14-0324.1.

Kogure, M., T. Nakamura, M. K. Ejiri, T. Nishiyama, Y. Tomikawa, and M. Tsutsumi, 2018: Effects of horizontal wind structure on a gravity wave event in the middle atmosphere over Syowa (69°S, 40°E), the Antarctic. *Geophys. Res. Lett.*, **45**, 5151–5157. doi:10.1029/2018GL078264.

Kruse, C. G., M. J. Alexander, L. Hoffmann, A. van Niekerk, I. Polichtchouk, J. T. Bacmeister, L. Holt, R. Plougonven, P. Šácha, C. Wright, K. Sato, R. Shibuya, S. Gisinger, M. Ern, C. I. Meyer, & O. Stein, 2022: Observed and modeled mountain waves from the surface to the mesosphere near the Drake Passage. *J. Atmos. Sci.*, **79(4)**, 909-

932. doi:10.1175/JAS-D-21-0252.1.

McFarlane, N. A., 1987: The effect of orographically excited gravity wave drag on the general circulation of the lower stratosphere and troposphere. *J. Atmos. Sci.*, **44**, 1775–1800. doi:10.1175/1520-0469(1987)044<1775:TEOOEG>2.0.CO;2.

McLandress, C., T. G. Shepherd, S. Polavarapu, and S. R. Beagley, 2012: Is missing orographic gravity wave drag near 60°S the cause of the stratospheric zonal wind biases in chemistry–climate models? *J. Atmos. Sci.*, **69**, 802–818. doi:10.1175/JAS-D-11-0159.1.

Mihalikova, M., K. Sato, M. Tsutsumi, and T. Sato, 2016: Properties of inertia-gravity waves in the lowermost stratosphere as observed by the PANSY radar over Syowa Station in the Antarctic. *Ann. Geophys.*, **34**, 543–555. doi:10.5194/angeo-34-543-2016.

Minamihara, Y., K. Sato, and M. Tsutsumi, 2020: Intermittency of gravity waves in the Antarctic troposphere and lower stratosphere revealed by the PANSY radar observation. *J. Geophys. Res. Atmos.*, **125(15)**, e2020JD032543. doi:10.1029/2020JD032543.

Minamihara, Y., K. Sato, M. Tsutsumi, and T. Sato, 2018: Statistical characteristics of gravity waves with near-inertial frequencies in the Antarctic troposphere and lower stratosphere observed by the PANSY radar. *J. Geophys. Res.: Atmos.*, **123(17)**, 8993–9010. doi:10.1029/2017JD028128.

Okui, H., K. Sato, D. Koshin, and S. Watanabe, 2021: Formation of a mesospheric inversion layer and the subsequent elevated stratopause associated with the major stratospheric sudden warming in 2018/19. *J. Geophys. Res.: Atmos.*, **126**, e2021JD034681. doi:10.1029/2021JD034681.

Palmer, T. N., G. J. Shutts, and R. Swinbank, 1986: Alleviation of a systematic westerly bias in general circulation and numerical weather prediction models through an orographic gravity wave drag parametrization. *Quart. J. Roy. Meteor. Soc.*, **112**: 1001-1039. doi:10.1002/qj.49711247406.

Pfenninger, M., A. Z. Liu, G. C. Papen, and C. S. Gardner, 1999: Gravity wave characteristics in the lower atmosphere at south pole. *J. Geophys. Res.: Atmos.*, **104(D6)**, 5963–5984. doi:10.1029/98JD02705.

Plougonven, R., V. Jewtoukoff, A. Cámara, F. Lott, and A. Hertzog, 2017: On the relation between gravity waves and wind speed in the lower stratosphere over the Southern Ocean. *J. Atmos. Sci.*, **74(4)**, 1075–1093. doi:10.1175/JAS-D-16-0096.1.

Plougonven, R., and C. Snyder, 2007: Inertia–gravity waves spontaneously generated by jets and fronts. Part I: different baroclinic life cycles. *J. Atmos. Sci.*, **64** 2502–2520. doi:10.1175/jas3953.1.

Plumb, R. A., 2002: Stratospheric transport. *J. Meteor. Soc. Japan Ser. II*, **80(4B)**, 793–809. doi:10.2151/jmsj.80.793.

Sato, K., 1994: A statistical study of the structure, saturation and sources of inertio-gravity waves in the lower stratosphere observed with the MU radar. *J. Atmos. Terr. Phys.*, **56(6)**, 755–774. doi:10.1016/0021-9169(94)90131-7.

Sato, K., and T. J. Dunkerton, 1997: Estimates of momentum flux associated with equatorial Kelvin and gravity waves. *J. Geophys. Res.: Atmos.*, **102(D22)**, 26247-26261. doi:10.1029/96JD02514.

Sato, K., and N. Hirasawa, 2007: Statistics of Antarctic surface meteorology based on hourly data in 1957-2007 at Syowa Station. *Polar Sci.*, **1**, 1–15. doi:10.1016/j.polar.2007.05.001.

Sato, K., M. Kohma, M. Tsutsumi, and T. Sato, 2017: Frequency spectra and vertical profiles of wind fluctuations in the summer Antarctic mesosphere revealed by MST radar observations. *J. Geophys. Res.: Atmos.*, **122**, 3–19. doi:10.1002/2016JD025834.

Sato, K., D. J. O'Sullivan, and T. J. Dunkerton, 1997: Low-frequency inertia-gravity waves in the stratosphere revealed by three-week continuous observation with the MU radar, *Geophys. Res. Lett.*, **24**, 1739–1742. doi:10.1029/97GL01759.

Sato, K., S. Tateno, S. Watanabe, and Y. Kawatani, 2012: Gravity wave characteristics in the Southern Hemisphere revealed by a high-resolution middle-atmosphere general circulation model. *J. Atmos. Sci.*, **69**, 1378–1396. doi:10.1175/JAS-D-11-0101.1.

Sato, K., M. Tsutsumi, T. Sato, T. Nakamura, A. Saito, Y. Tomikawa, K. Nishimura, M. Kohma, H. Yamagishi and T. Yamanouchi, 2014: Program of the Antarctic Syowa MST/IS Radar (PANSY). *J. Atmos. Sol.-Terr. Phys.,* **118, PartA,** 2-15, doi:10.1016/j.jastp.2013.08.022.

Sato, K., and M. Yoshiki, 2008: Gravity wave generation around the polar vortex in the stratosphere revealed by 3-hourly radiosonde observations at Syowa Station. *J. Atmos. Sci.*, **65**, 3719–3735. doi:10.1175/2008JAS2539.1.

Sato, K., S. Watanabe, Y. Kawatani, Y. Tomikawa, K. Miyazaki, and M. Takahashi, 2009: On the origins of mesospheric gravity waves. *Geophys. Res. Lett.*, **36(19)**, L19801. doi:10.1029/2009GL039908.

Sutherland, B., and K. Yewchuk, 2004: Internal wave tunneling. *J. Fluid Mech.*, **511**, 125–134. doi:10.1017/S0022112004009863.

Vincent, R. A., and I. M. Reid, 1983: HF Doppler measurements of mesospheric gravity wave momentum fluxes. *J. Atmos. Sci.*, **40(5)**, 1321–1333. doi:10.1175/1520-0469(1983)040<1321:HDMOMG>2.0.CO;2.

Yasuda, Y., K. Sato, and N. Sugimoto, 2015: A theoretical study on the spontaneous radiation of inertia-gravity waves using the renormalization group method. Part I: derivation of the renormalization group equations. *J. Atmos. Sci.*, **72**, 957–983. doi:10.1175/JAS-D-13-0370.1.

Yasuda, Y., K. Sato, and N. Sugimoto, 2015: A theoretical study on the spontaneous radiation of inertia-gravity waves using the renormalization group method. Part II: verification of the theoretical equations by numerical simulation. *J. Atmos. Sci.*, **72**, 984–1009. doi:10.1175/JAS-D-13-0371.1.

Yoo, J. H., T. Choi, H. Y. Chun, Y. H. Kim, I. S. Song, and B. G. Song, 2018: Inertia-gravity waves revealed in radiosonde data at Jang Bogo Station, Antarctica (74°37′S, 164°13′E): 1. Characteristics, energy, and momentum flux. *J. Geophys. Res. Atmos.*, **123**, 13–305. doi:10.1029/2018JD029164.

Yoshiki, M., N. Kizu, and K. Sato, 2004: Energy enhancements of gravity waves in the Antarctic lower stratosphere associated with variations in the polar vortex and tropospheric disturbances. *J. Geophys. Res.: Atmos.*, **109**, D23104. doi:10.1029/2004JD004870.

Yoshiki, M., and K. Sato, 2000: A statistical study of gravity waves in the polar regions based on operational radiosonde data. *J. Geophys. Res.*, **105(D14)**, 17995–18011. doi:10.1029/2000JD900204.

List of Figures

vertical kinetic energy $\mathrm{KE}_{(z)}$, (e) the ratio of the vertical kinetic energy to the horizontal kinetic energy R, (f) ratio of the Coriolis parameter to the intrinsic frequency $f/\hat{\omega}$, and (g) the ratio of the horizontal wave number to the vertical wave number k/m. The contours of (a) and (b) indicate the background field of zonal ($\bar{u}$) and meridional ($\bar{v}$) wind. The contour intervals are 5 $\mathrm{m/s}$ and 2.5 $\mathrm{m/s}$.

Fig. 5 (a–b) Time-height sections of the vertical flux divergence of the horizontal momentum for the short wave period GWs. Time-height sections of (a) the divergence of the vertical flux of zonal momentum $-\frac{1}{\rho_0}\frac{\partial \rho_0 \overline{u'w'}}{\partial z}$, and (b) the divergence of the vertical flux of meridional momentum $-\frac{1}{\rho_0}\frac{\partial \rho_0 \overline{v'w'}}{\partial z}$. The contours of (a) and (b) indicate the background field of zonal ($\bar{u}$) and meridional ($\bar{v}$) wind. The contour intervals are 5 $\mathrm{m/s}$ and 2.5 $\mathrm{m/s}$. (c–d) The vertical profiles for the vertical flux divergences of the horizontal momentum and their standard deviations. The vertical profiles for (c) the vertical flux divergence of zonal momentum $-\frac{1}{\rho_0}\frac{\partial \rho_0 \overline{u'w'}}{\partial z}$ and (d) the vertical flux divergence of meridional momentum $-\frac{1}{\rho_0}\frac{\partial \rho_0 \overline{v'w'}}{\partial z}$. The solid and dashed lines of (c) and (d) indicate the time-mean momentum flux divergences and their standard deviations.

Fig. 6 Same as Fig. 4, but due to short vertical wavelength GWs.

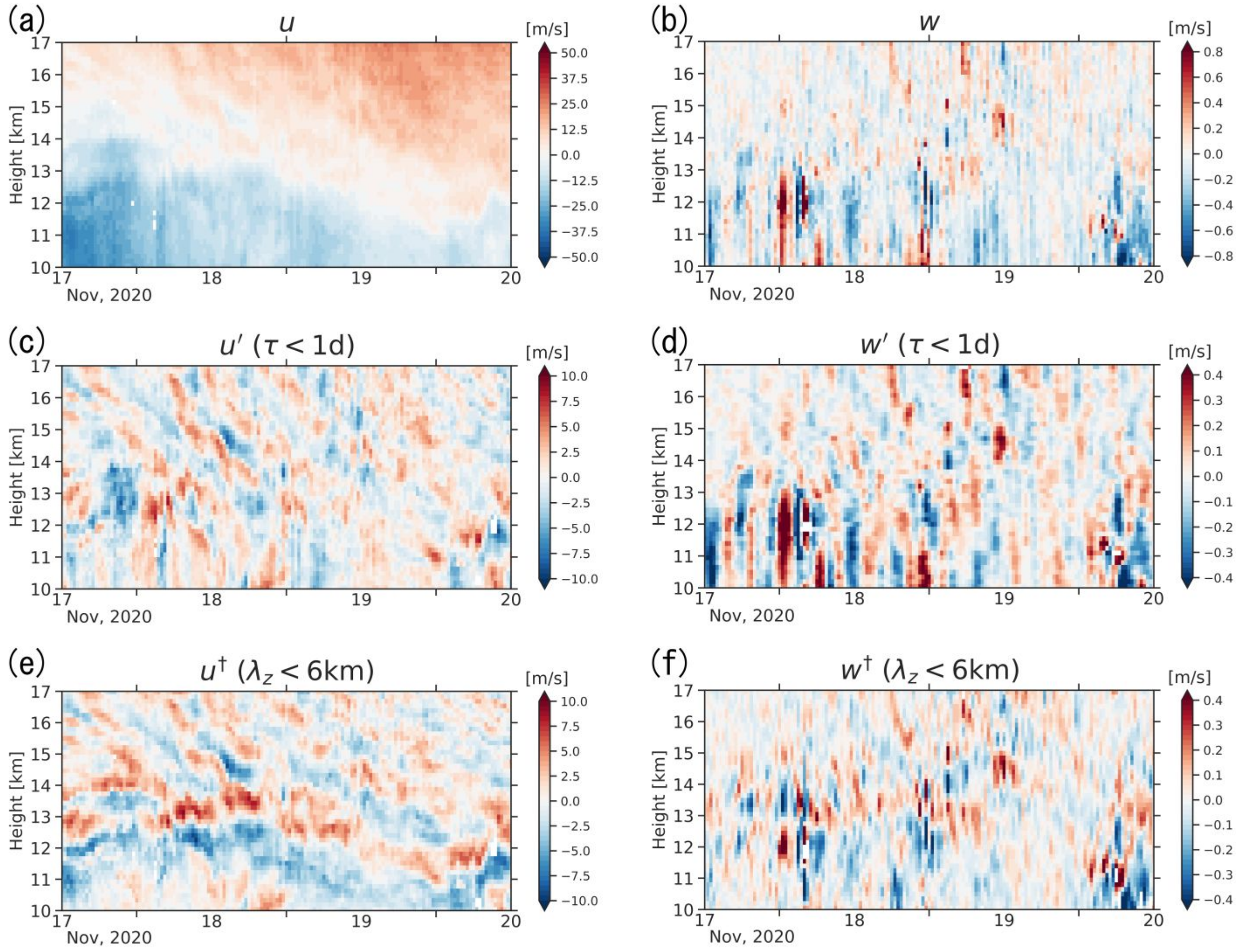

Fig. 1 Time-height sections of (a) u and (b) w in the altitude range of 10–17 km from 12UTC 17 to 12UTC 20 November 2020. (c) and (d) Same as (a) but for fluctuations with wave periods shorter than 1 day. (e) and (f) Same as (a) but for fluctuations with vertical wavelengths shorter than 6 km.

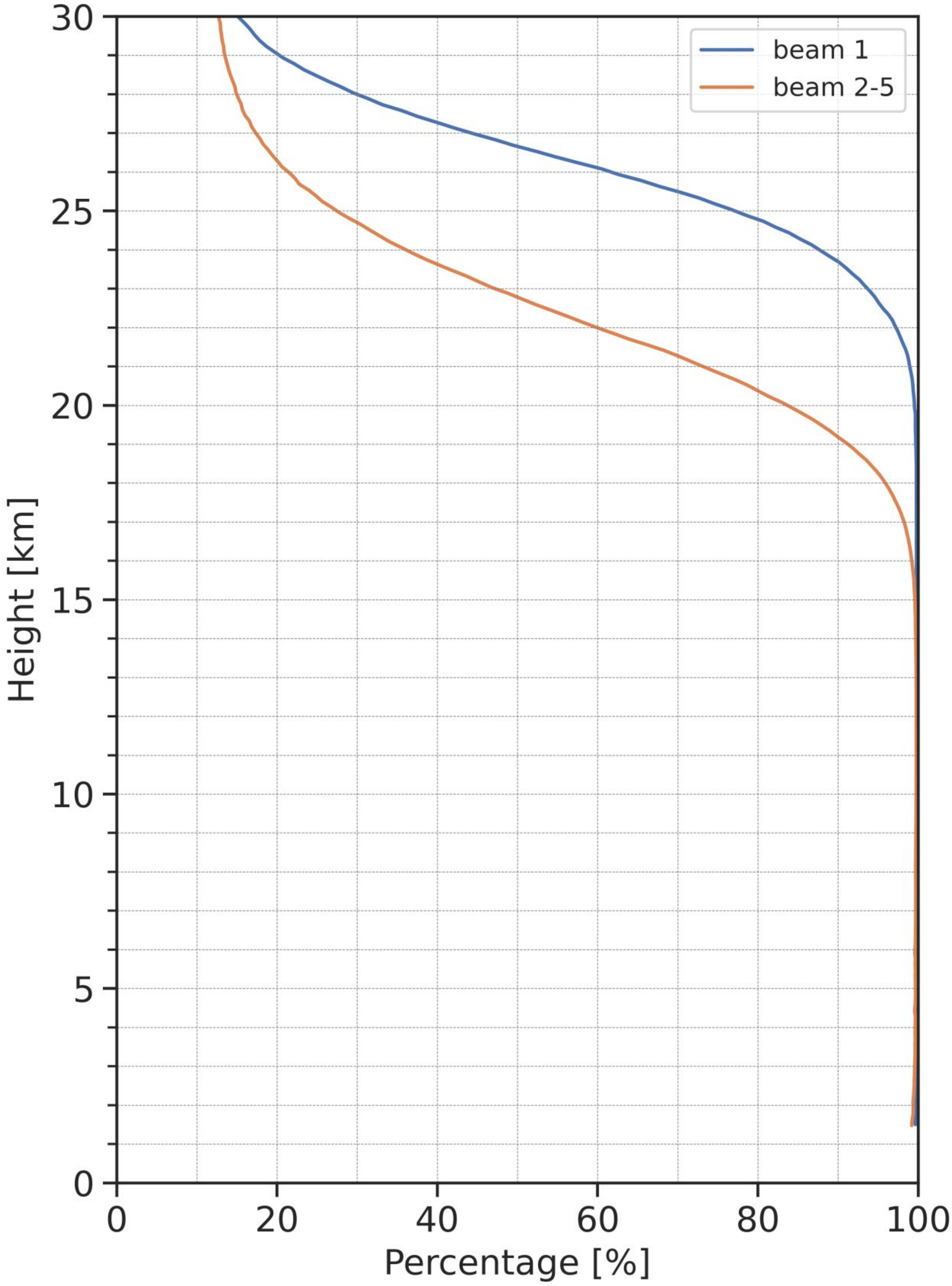

Fig. 2 Vertical profiles of the percentage of effective observation points for the vertical beam (blue) and oblique beams (orange).

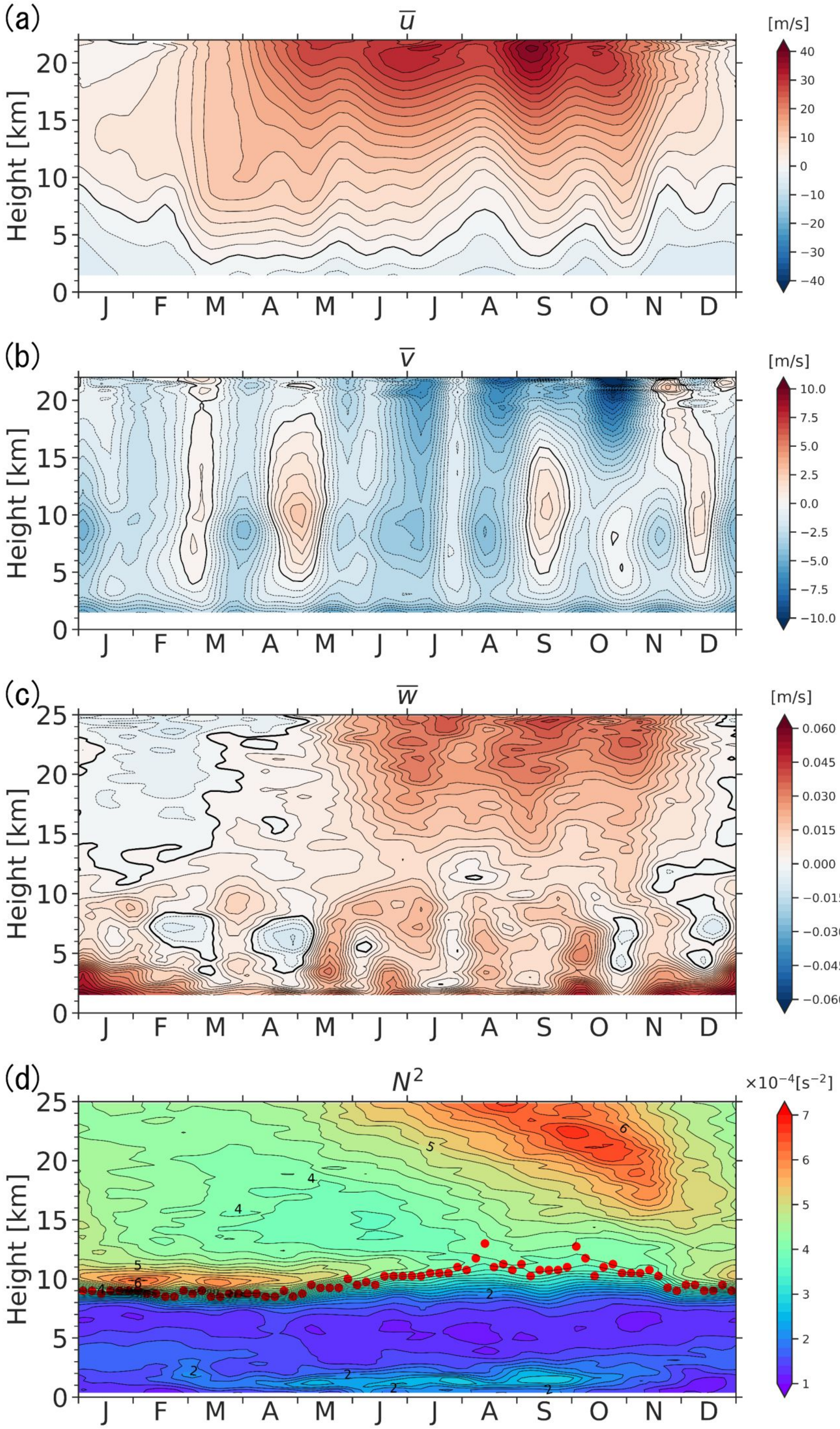
(a)
$\overline{u}$
[m/s]
Height [km]
J F M A M J J A S O N D
(b)
$\overline{v}$
[m/s]
(c)
$\overline{w}$
[m/s]
(d)
N^2
$\times10^{-4}[s^{-2}]$

608

Fig. 3 (a)Time-height sections of the climatological mean of the background field of zonal wind $\overline{u}$. The contour interval is 2 $\mathrm{m/s}$. The thick line indicates 0 $\mathrm{m/s}$. (b)Same as (a) but for meridional wind $\overline{v}$. The contour interval is 0.5 $\mathrm{m/s}$. (c)Same as (a) but for vertical wind $\overline{w}$. The contour interval is 0.003 $\mathrm{m/s}$. (d)Same as (a) but for Brunt-Väisälä frequency squared N^2 with the tropopause (red circles) for the climatological mean temperature. The contour interval is $2 \times 10^{-5}\ \mathrm{s}^{-2}$.

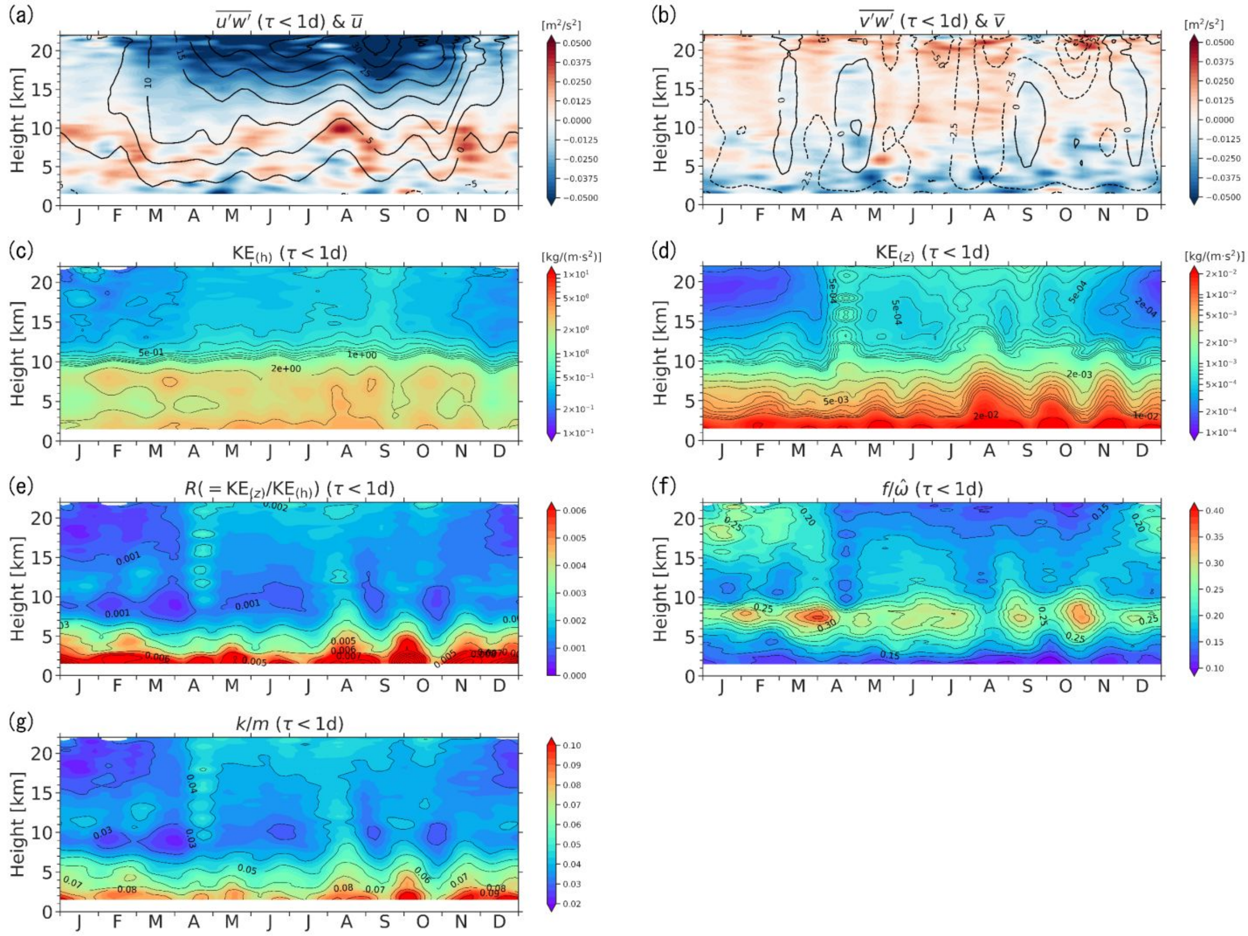

Fig. 4 (a–g) Time-height sections of climatology of wave characteristics of the short wave period GWs. Time-height sections of (a) the vertical flux of zonal momentum $\overline{u'w'}$, (b) the vertical flux of meridional momentum $\overline{v'w'}$, (c) the horizontal kinetic energy $\mathrm{KE}_{(\mathrm{h})}$, (d) the vertical kinetic energy $\mathrm{KE}_{(z)}$, (e) the ratio of the vertical kinetic energy to the horizontal kinetic energy R, (f) ratio of the Coriolis parameter to the intrinsic frequency $f/\hat{\omega}$, and (g) the ratio of the horizontal wave number to the vertical wave number k/m. The contours of (a) and (b) indicate the background field of zonal ($\bar{u}$) and meridional ($\bar{v}$) wind. The contour intervals are 5 $\mathrm{m/s}$ and 2.5 $\mathrm{m/s}$.

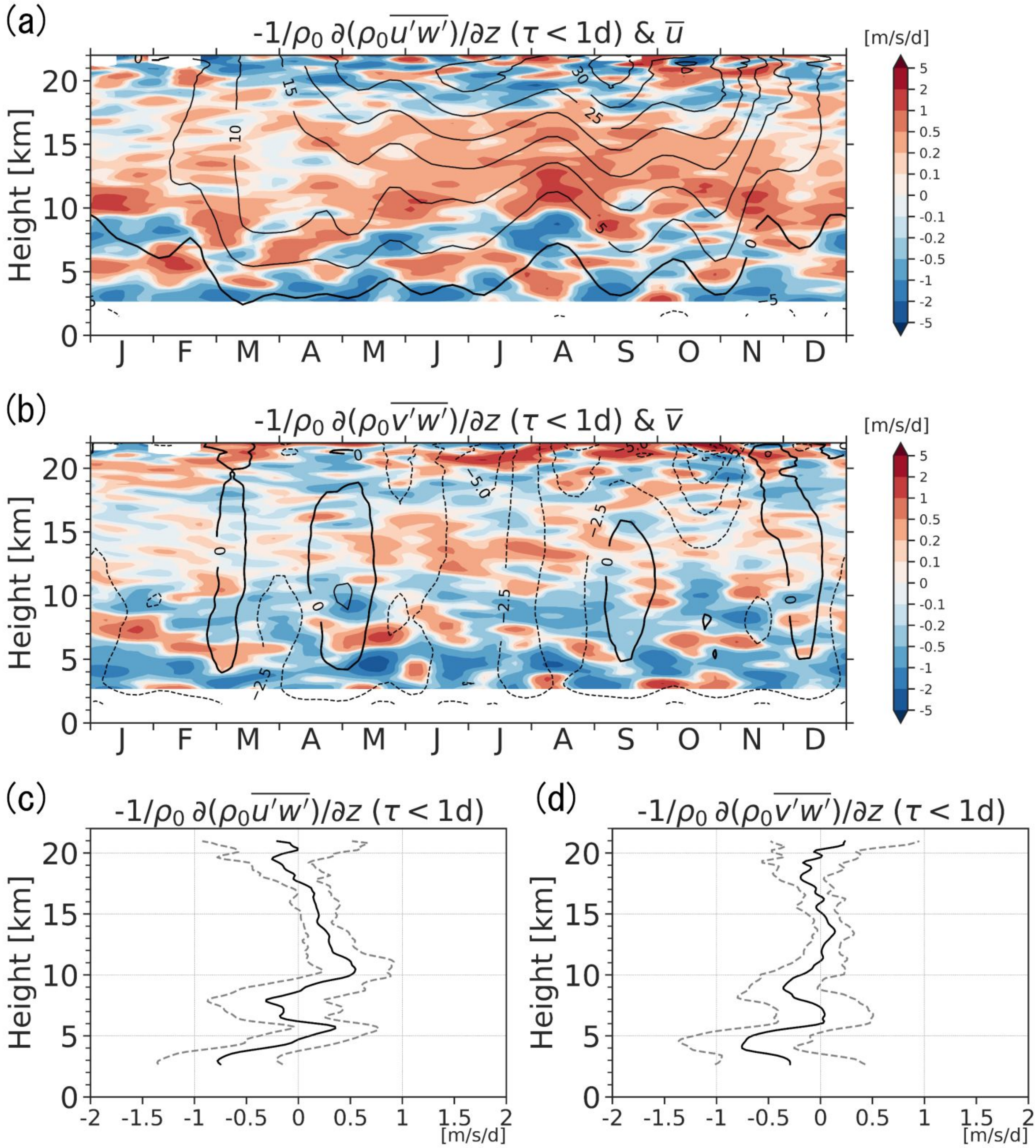

Fig. 5 (a–b) Time-height sections of the vertical flux divergence of the horizontal momentum for the short wave period GWs. Time-height sections of (a) the divergence of the vertical flux of zonal momentum $-\frac{1}{\rho_0}\frac{\partial \rho_0 \overline{u'w'}}{\partial z}$, and (b) the divergence of the vertical flux of meridional momentum $-\frac{1}{\rho_0}\frac{\partial \rho_0 \overline{v'w'}}{\partial z}$. The contours of (a) and (b) indicate the background field of zonal ($\overline{u}$) and meridional ($\overline{v}$) wind. The contour intervals are 5 $\mathrm{m/s}$ and 2.5 $\mathrm{m/s}$. (c–

d) The vertical profiles for the vertical flux divergences of the horizontal momentum and their standard deviations. The vertical profiles for (c) the vertical flux divergence of zonal momentum $-\frac{1}{\rho_0}\frac{\partial \rho_0 \overline{u'w'}}{\partial z}$ and (d) the vertical flux divergence of meridional momentum $-\frac{1}{\rho_0}\frac{\partial \rho_0 \overline{v'w'}}{\partial z}$. The solid and dashed lines of (c) and (d) indicate the time-mean momentum flux divergences and their standard deviations.

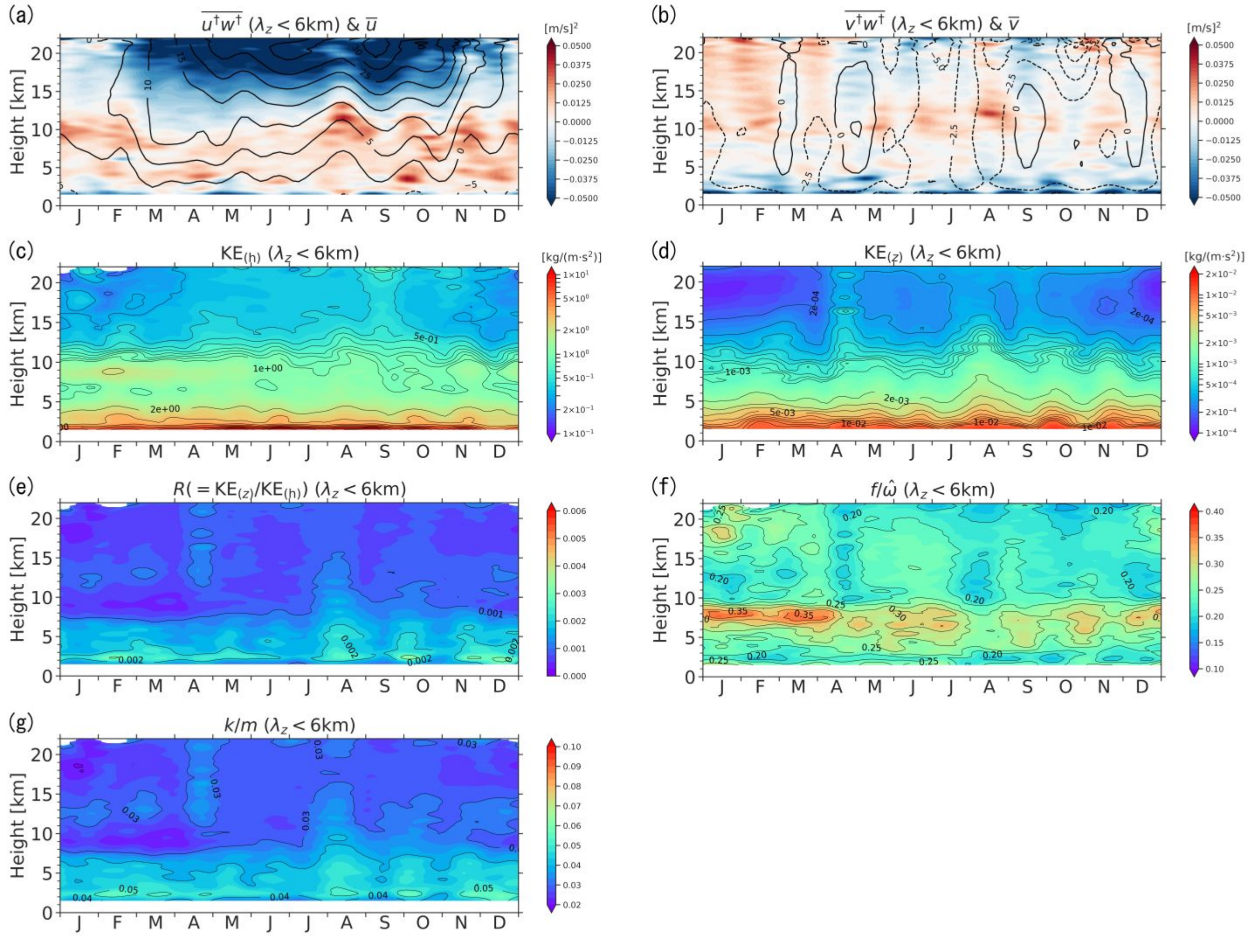

Fig. 6 Same as Fig. 4, but due to short vertical wavelength GWs.